Academic Science Journal

Study the Structural, Morphological and Magnetic Properties of (Bi Ni Fe_2 O_4/C) Nano Composite

Ahmed G. Awni and Zena M. Ali Abbas

Department of Physics, College of Science, University of Diyala

amongahmed972@gmail.com

Received: 21 June 2023 **Accepted: 11 August 2023**

DOI: https://doi.org/10.24237/ASJ.02.02.781B

Abstract

In this work, bismuth nickel ferrite (Bi_x Ni_{1-x} Fe_2O_4) supported by activated carbon (AC) with x=0, 0.3 and 0.5 were made and studied using the sol-gel method, and the samples were calcinated at 350 and 650 °C for 3 hours. XRD, FTIR, FESEM, and EDX spectroscopy were used to examine the chemical structure and morphology of bismuth nickel ferrite on activated carbon (Bi_x Ni_{1-x} Fe_2O_4/ C). The XRD patterns show that when the temperature of the synthesized material is raised, the intensity and spread of the peaks decrease. This leads to more crystallization. FTIR studies were done in the frequency range (400–4000) cm^{-1}, and the FTIR spectrum of (Bi_x Ni_{1-x} Fe_2O_4/ C) shows the two significant absorption bands near the frequency ranges 500 cm^{-1} and 700 cm^{-1}. FESEM with particles that were between 17 and 60 nm in size was used to study the surface morphology. The EDS plots revealed the existence of no extra peaks other than constituents of the taken up composition. The decrease in saturation magnetization (M_s) and remanence magnetization (M_r) is seen through the utilization of a vibrating sample magnetometer (VSM).

Keywords: Activated Carbon , Sol-Gel Method, XRD, FTIR, FESEM, VSM.

دراسة الخواص التركيبية والمورفولوجيا والمغناطيسية للمركب النانوي (Bi Ni Fe_2 O_4/C)

أحمد غانم عوني و زينة محمد علي عباس

قسم الفيزياء - كلية العلوم - جامعة ديالى

Academic Science Journal

الخلاصة

في هذا العمل, تم صنع فرايت النيكل البزموث ($Bi_x Ni_{1-x} Fe_2O_4$) المدعوم بالكاربون المنشط (AC) حيث (x= 0, 0.3 ,0.5) بطريقة المحلول الغروي, تم تسخين العينات عند (350, 650) سيليزي لمدة 3 ساعات, تم استخدام التحليل الطيفي XRD, FTIR, FESEM وEDX لفحص التركيب الكيميائي والمورفولوجي والمغناطيسية لـ ($Bi_x Ni_{1-x} Fe_2O_4$/ C) . توضح انماط (XRD) انه عند ارتفاع درجة الحرارة نلاحظ تقليل شدة وتوسيع القمم وهذا يؤدي الى مزيدا من التبلور, اجريت دراسة FTIR ضمن نطاق تردد (400-4000) سم$^{-1}$ حيث اظهر طيف (FTIR) لـ نطاقي امتصاص بارزين عند الترددات (500و700) سم$^{-1}$, تم استخدام التشكل السطحي بواسطة (FESEM) وكانت حجم الجسيمات (17-60)نانومتر , كشفت انماط (EDX) عن عدم وجود قمم اضافية بخلاف مكونات المركب المستخدم. لوحظ ضعف في التفاعل المغناطيسي بين الكاتيونات باستخدام نموذج الاهتزاز المغناطيسي (VSM) ، مما تسبب في انخفاض التشبعية المغناطيسية (M_s) و التخلفية المغناطيسية (M_r)

الكلمات المفتاحية: الكاربون المنشط, طريقة المحلول الغروي, حيود الاشعة السينية, تحويلات فوريه للاشعة تحت الحمراء, المجال الباعث للمجهر الالكتروني الماسح, نموذج الاهتزاز المغناطيسي

Introduction

Among the many beneficial qualities of carbon-based materials and conductive polymers are their high dielectric constants and low densities. Although graphite was one of the earliest absorbents to be put to use, other carbon-based materials, including carbon black [1], carbon fibers [2], and carbon nanotubes [3], have all seen extensive applications as well. In order to maximize absorption, researchers have studied the effects of doping or altering carbon and inorganic magnetic elements in composites [4, 5]. Activated carbons are a popular material for photocatalyst supports because they have high specific surface areas, are easy to control in terms of surface chemistry, are good at absorbing organic compounds, have high porosity, and can be burned to recover the active metal phase. The porous nature of the carbon allows molecules of a pollutant that have been absorbed to reach the photo-catalytically active sites. This increases the rate of oxidative breakdown under UV light, which suggests that the carbon support may have its own photoactivity [2]. Spinel ferrites (MFe_2O_4, where M = Ni, Mg, Ca, or Co) have narrow band gaps (2.0 eV), magnetic separation, and chemical stability that make their nanoparticles great options for use as photocatalysts in decontaminating the environment

[6,7]. Attractive to scientists is the prospect of using magnetic semiconductor nanoparticles in water purification. Nickel ferrites with the general formula (AB_2O_4) are among the most valuable magnetic materials due to their high curie temperature, strong saturation magnetization, chemical stability, and relatively high permeability [8].

Experimental

Synthesis of the bismuth nickel ferrite-activated carbon samples

The purity of the nickel nitrate, iron nitrate, bismuth nitrate, and carbon was 99%. A pH meter, an industrial oven, and an Ohaus digital weighing scale were also used. The bismuth nickel ferrite-activated carbon (AC) materials having different compositions [$Ni\ Fe_2O_4$/ C], [$Bi_{0.3}\ Ni_{0.7}\ Fe_2O_4$/C], and [$Bi_{0.5}\ Ni_{0.5}\ Fe_2O_4$/C], (denoted as S, S1 and S2) calcined at 350 ^oC and [$Ni\ Fe_2O_4$/C], [$Bi_{0.3}\ Ni_{0.7}\ Fe_2O_4$/C] and [$Bi_{0.5}\ Ni_{0.5}\ Fe_2O_4$/C], (denoted as S3, S4 and S5) calcined at 650 ^oC. More details are in Table (1). Drops of ammonia solution were slowly added to the mixed solution while it was being stirred constantly to control its pH, this was done until it hit a value of pH=7 and turned a dark brown color. Stir for 30 minutes at room temperature to blend everything. Raise the temperature to 90°C gradually. Stir continuously until gel forms. After 30 minutes, the solution's viscosity is very high, so gel formation begins on the surface, notably in the middle, and eventually all of it gels. The solution remains on the magnetic stirrer at 90 °C. The burned gel becomes a fine, dark gray powder. High-purity ferrite production has commenced.

Table 1. Details of the symbols used.

SAMPLE NAME	MATERIAL	CALCINATION TEMPERATURE (^OC)
S	$Ni\ Fe_2O_4$ /C	350^OC
S1	$Bi_{0.3}Ni_{0.7}\ Fe_2O_4$/C	350^OC
S2	$Bi_{0.5}\ Ni_{0.5}\ Fe_2O_4$/C	350^OC
S3	$Ni\ Fe_2O_4$ /C	650^OC
S4	$Bi_{0.3}\ Ni_{0.7}\ Fe_2O_4$/C	650^OC
S5	$Bi_{0.5}Ni_{0.5}\ Fe_2O_4$/C	650^OC

Characterization

The structural characteristics of (Bi_x Ni_{x-1} Fe_2O_4 /C) nanoparticles have been studied by the XRD type (Panalytical X' Pert Pr, UK) and the FTIR type (IR Affinty-1CE (FTIR) spectrophotometer). The morphological characteristics have been studied by field emission scanning electron microscope (FESEM) and model (ZEISS SIGMAVP/Germany). Vibrating sample magnetometer (VSM) using the (LBKFB Meghnatis Daghigh Kavir Company model).

Results and Discussion

XRD Analysis

Figure (1a) shows the XRD pattern of activated carbon, which has a clear, broad peak at 2θ= 25.17°, 2θ=43.51º, and a weak peak at 2θ=29.4°, 2θ=39.9º, which match the (002), (400) and (220), (100) crystallographic planes, respectively. The measured peaks were linked to activated carbon with hexagonal crystals [9,10] correspond to (ICDD: 00–041-1987). Figure 1(b,c) shows the XRD patterns of $NiFe_2O_4$/ AC at (350 and 650)ºC ,respectively. $NiFe_2O_4$/ AC exhibited spinel diffraction peaks at 2θ values of 30.49°, 35.68°, 37.33°, 43.53°,57.45°, and 63.02° which correspond to crystallographic. Finally, $NiFe_2O_4$/ AC has diffraction peaks at 2θ = 30.49°(220), 35.68° (311), 37.33° (222), 43.53° (400), 57.45° (511), and 63.02° (440) [11] (ICDD: 00–010-0325). When different types of Bi Ni Fe_2O_4 were deposited on the surface of the alternating current, we notice a decrease in the strength of the carbon peaks with the emergence of other peaks. The appearance of these peaks is attributed to the interaction of metal oxides with the alternating current [12]. Activated carbon proves that $NiFe_2O_4$ nanoparticles can form and persist. The crystallite size (D) is calculated using Scherrer's formula [13]:

$$D=k\,\lambda_x/\beta\cos\theta \qquad (1)$$

Where k: is shape factor. λ_x: is the wavelength of incident x-ray radiation = (1.5406 Å for CuKα). β: is the full width at half maximum (FWHM) of the peak (in radians). θ: is Bragg's angle, and Table 2 shows that the crystallite size of Bi $NiFe_2O_4$/C nanoparticles decreased with the rise in nickel ferrites concentration.

Academic Science Journal

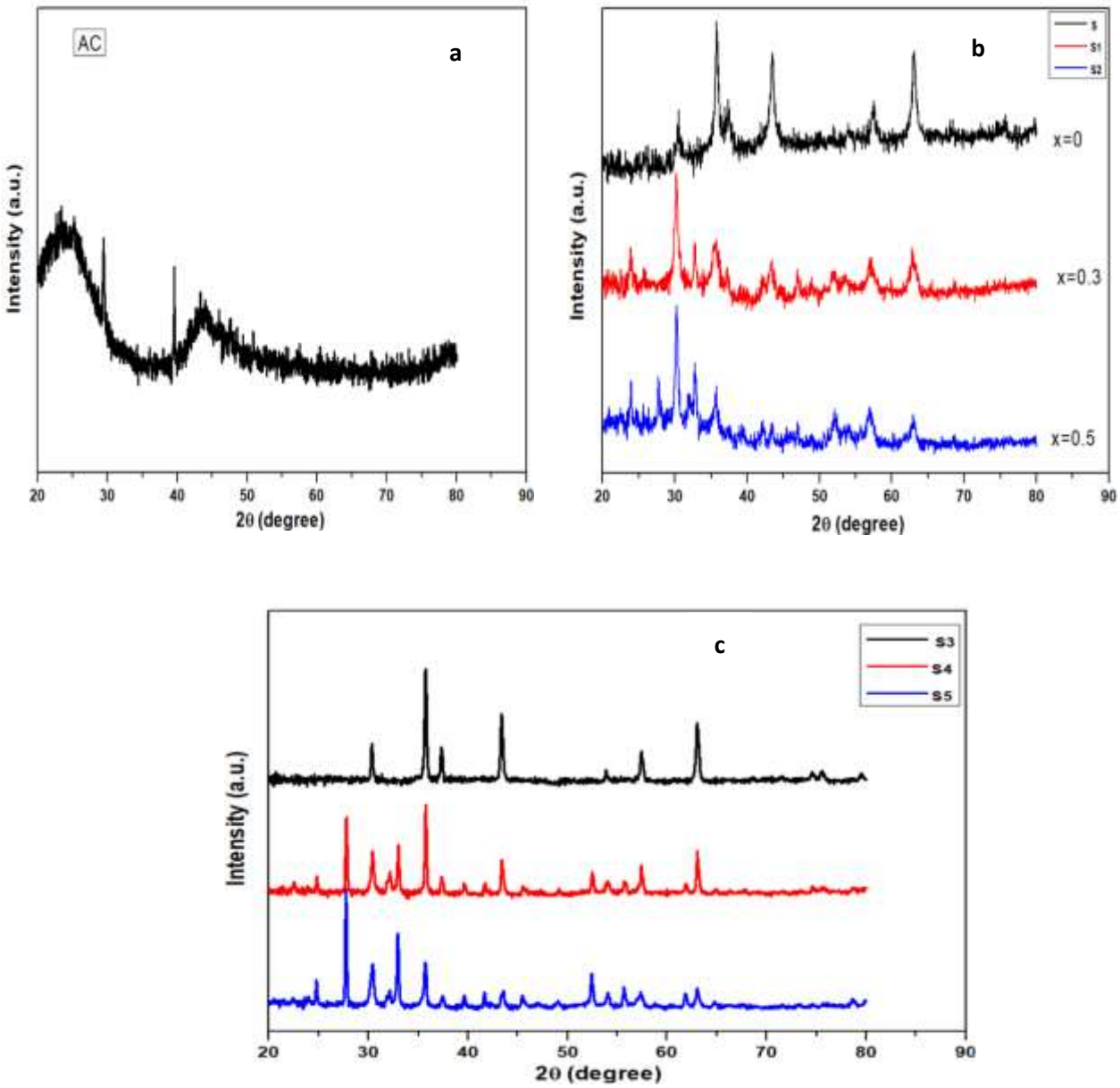

Figure 1: The XRD pattern of $Bi_x Ni_{1-x}Fe_2O_4$ /C (x = 0, 0.3 and 0.5) nano ferrite particles (a- AC , b- $Bi_x Ni_{1-x}Fe_2O_4$ /C calcined at 350 ºC and c- $Bi_x Ni_{1-x}Fe_2O_4$ /C calcined at 650 ºC).

Academic Science Journal

Table 2: XRD calculations of $Bi_x Ni_{1-x} Fe_2 O_4/C$ (x=0, 0.3, and 0.5) at different calcination temperatures (350 and 650)^oC.

Material	2Θ (deg) Practical	2Θ (deg) Standard	FWHM (deg)	Crystalline size (nm)	d hkl (A°) Practical	d_{hkl} (A°) Standard	(hkl)
AC	25.17	26.34	4.52	1.8017	3.53	3.38	(002)
	29.4	30.294	0.063159	130.1014	3.04	2.94	(220)
	39.9	41.22	0.106912	79.0886	2.27	2.13	(100)
	43.51	43.363	2.508430	3.4115	2.02	2.08	(400)
$Bi_x Ni_{1-x}Fe_2O_4$ /C calcined at (350 °C)	30.49	30.29	0.359323	22.94	2.93	2.94	(220)
	35.68	35.7	0.469630	17.8	2.51	2.51	(311)
	37.33	37.31	0.860051	9.75	2.40	2.4	(222)
	43.53	43.36	0.646653	13.24	2.08	2.08	(400)
	57.45	57.35	0.584515	18.68	1.604	1.6	(511)
	63.02	62.91	0.539753	12.55	1.47	1.47	(440)
$Bi_x Ni_{1-x}Fe_2O_4$ /C calcined at (650 °C)	30.33	30.29	0.175565	46.92	2.93	2.94	(220)
	35.74	35.7	0.185863	45.14	2.51	2.51	(311)
	37.33	37.31	0.179343	46.86	2.40	2.4	(222)
	43.38	43.36	0.184208	46.48	2.08	2.08	(400)
	53.89	53.8	0.185291	48.19	1.701	1.702	(422)
	57.4	57.35	0.200464	45.3	1.604	1.6	(511)
	62.99	62.91	0.217547	42.95	1.47	1.47	(440)

FTIR Analysis

The FTIR spectra of the as-prepared samples ($Bi_x Ni_{1-x} Fe_2 O_4/C$) are given in Figure (2). This spectrum comprises the characteristic peaks of activated carbon and nickel ferrite, which supports the synthesis of the composite material. The FTIR spectra of the materials made from ($Bi_x Ni_{1-x}Fe_2 O_4/C$) showed strong bands in the lower mid-infrared (500–700 cm-1) region. The stretching waves of the metal–oxygen bond (M–O; M = Ni and Fe) are thought to have caused these bands [14]. The (Fe–O) and (Ni–O) stretching vibration bands of ($Bi_x Ni_{1-x} Fe_2 O_4/C$) were thought to be the cause of the strong peaks found at 578 and 619 cm^{-1} [15, 16]. These strong peaks might also be related to the Fe-O vibration of octahedral spinel ferrite [17,18]. Each of the manufactured materials exhibits a peak in the region of 1550 cm^{-1} that can be attributed to (CO stretching) [16, 18]. Which is due to the fact that it was physisorbed in addition, the significant peak that was observed in the activated carbon at around 2000–2300 cm^{-1} could be due to an asymmetrical stretch of O=C=O that was trapped inside the pores of the activated carbon while the calcination process was taking place [19]. It has been determined

that the (N–H) stretching frequency of amide II is responsible for the absorption peak that occurs about 3850 cm^{-1} [9].

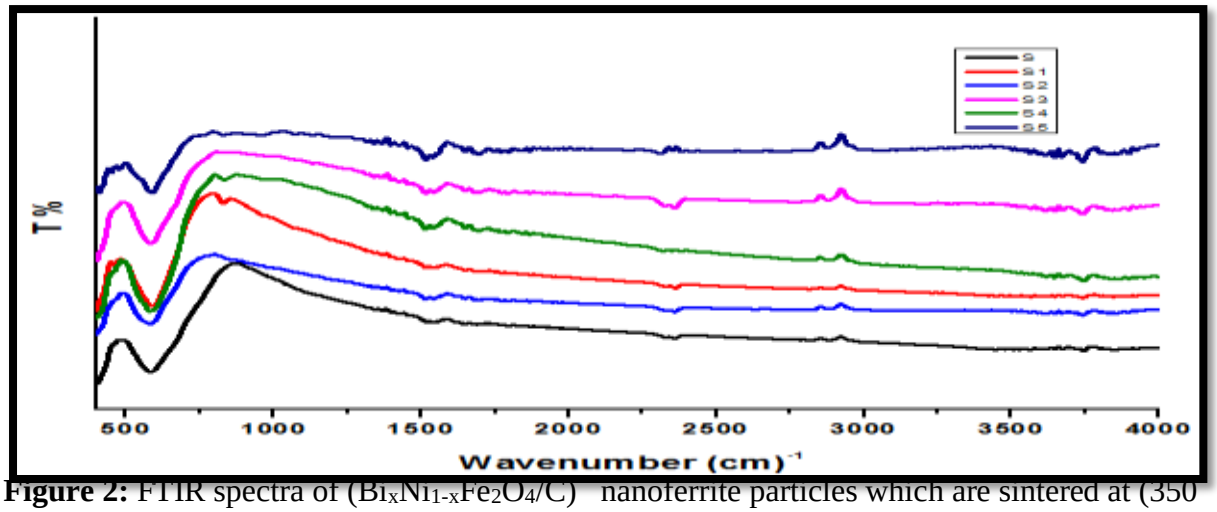

Figure 2: FTIR spectra of ($Bi_xNi_{1-x}Fe_2O_4$/C) nanoferrite particles which are sintered at (350 and 650) ° C

FESEM Analysis

Figure (3) shows the FESEM images analysis obtained for ($Bi_xNi_{1-x}Fe_2O_4$/C) composites. The morphology of each of the prepared samples reveals, to varying degrees, an aggregate of nanoparticles that are spherical and uniformly generated on the surface of the AC [14]. The use of AC as a support, generally, results in an improvement in the dispersion of transition metal oxides and a reduction in the agglomeration of such oxides [18]. The calcination process results in the emission of a significant amount of gas, which may be responsible for the presence of several fine pores or voids (defects) on the surface of the sample. According to the analysis of the micrograph, the size of the grains ranges from 17 to 60 nanometers. The FESEM images of the as-prepared composite (Bi_x Ni_{1-x} Fe_2 O_4/C) show that the activated carbon made from corncobs has a porous structure with numerous pores that are uniformly distributed across its surface. While making a composite out of bismuth nickel ferrite (Bi_x Ni_{1-x} Fe_2 O_4) particles and activated carbon, the ferrite particles were randomly distributed and devoured a portion of the surface porosity of the activated carbon. Although some of the AC porosity was shielded by (Bi_x Ni_{1-x} Fe_2 O_4) aggregates, the synthesized composite has its not porous structure on the AC

surface and has coated it. While we notice in the samples (S2, S4 and S5) the shape of the surface has changed from smooth to rough in texture.

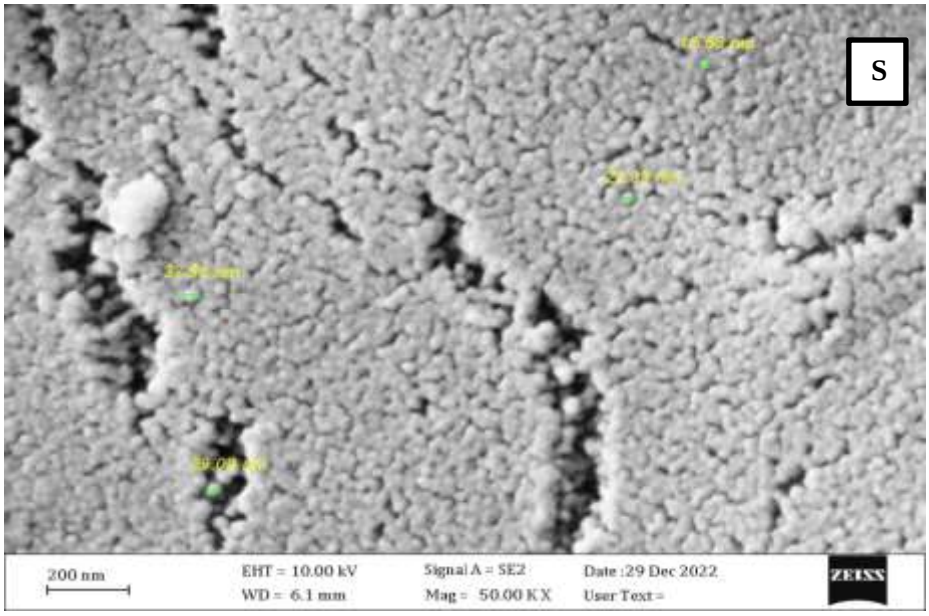

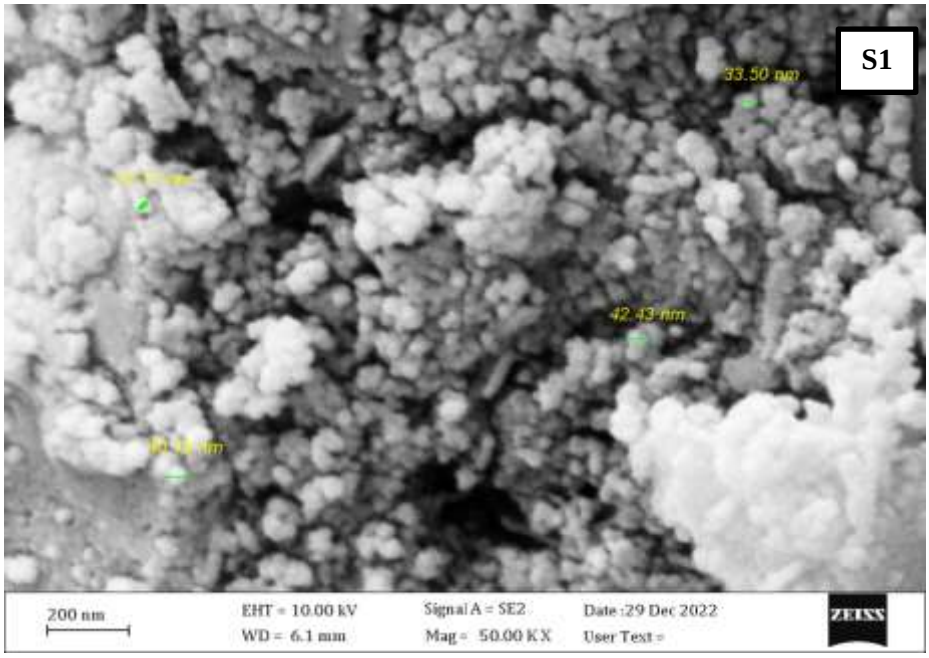

Academic Science Journal

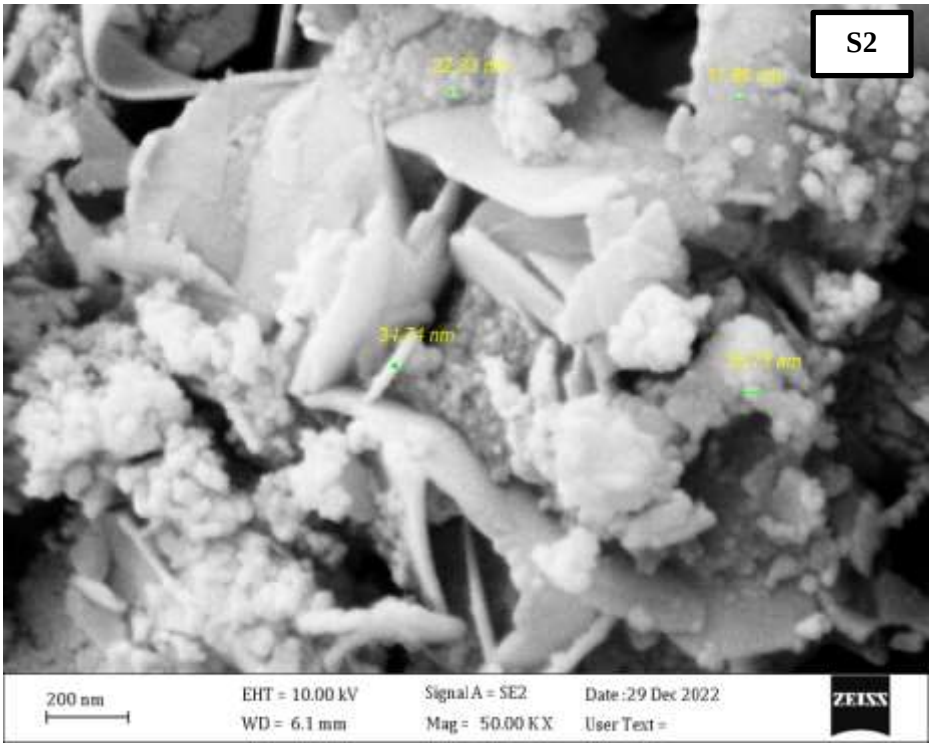

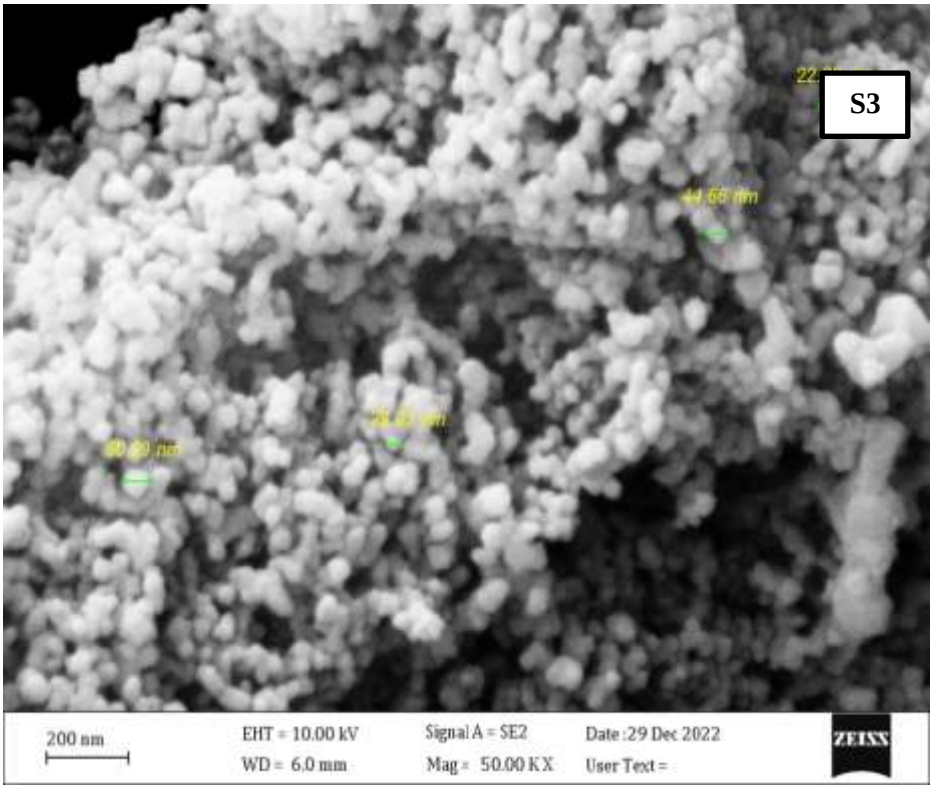

Academic Science Journal

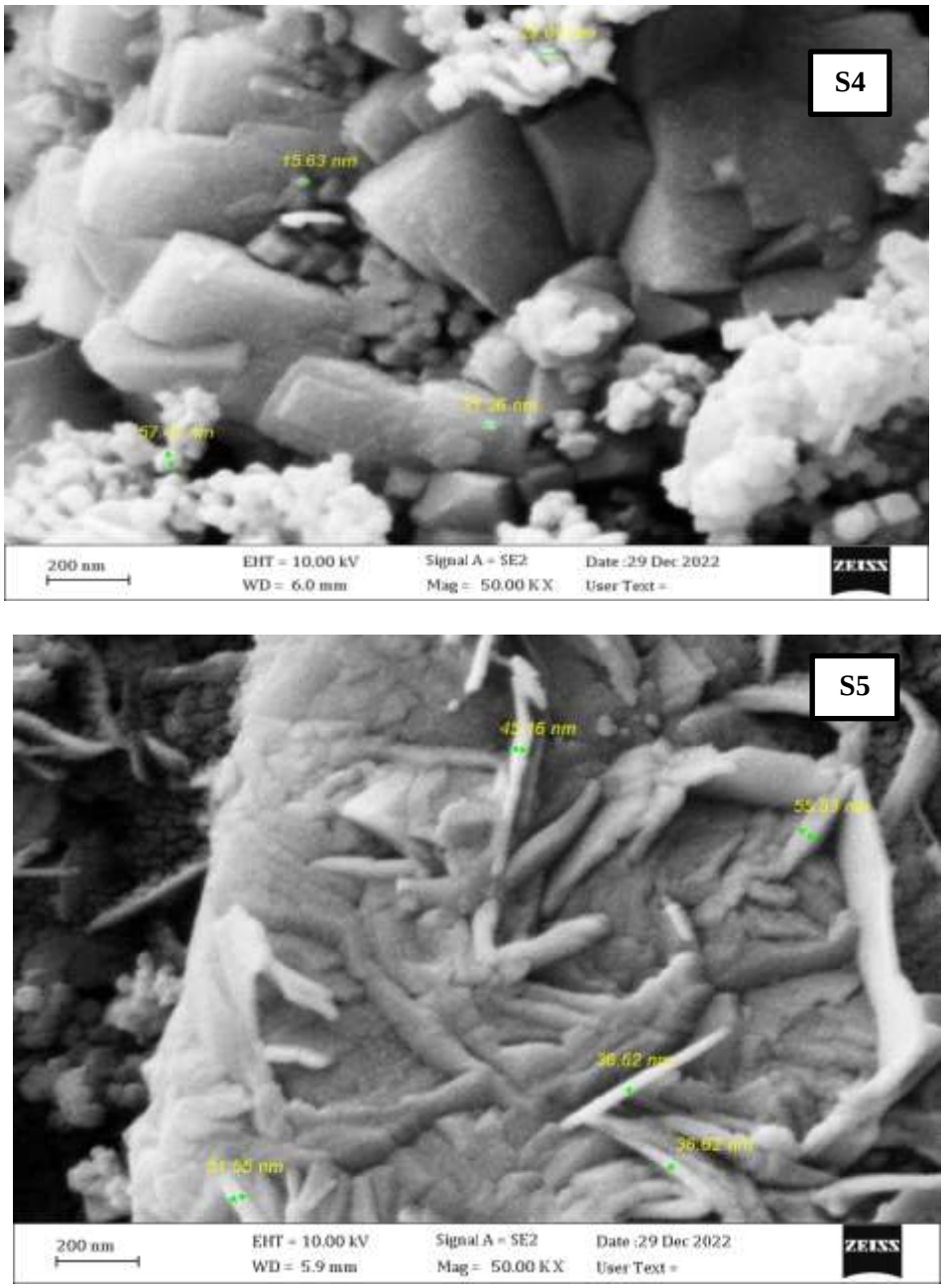

Figure 3: FESEM image of all ($Bi_xNi_{1-x}Fe_2O_4$/C) ferrite particles which are sintered at (350 and 650) ˚C

EDS Analysis

The EDX spectrum analysis reveals that the classic peaks of Bi, Fe, Ni, C, and O are present, that confirms the chemical structure of nanocomposite adsorbent. Figure (4,5) depicts a table

containing the weight percentages of the elements Bi, Fe, Ni, C, and O. This Table demonstrates that these components are present in the composites. This image demonstrates how spinels are formed. The constant elemental mappings reveal that O, Fe, C, Bi, and Ni are all spread out similarly. Carbon was the lowest fraction of all the chemicals created, indicating that metal-oxide layers covered the majority of the catalysts' surface [16]. These findings are supported by the FESEM values.

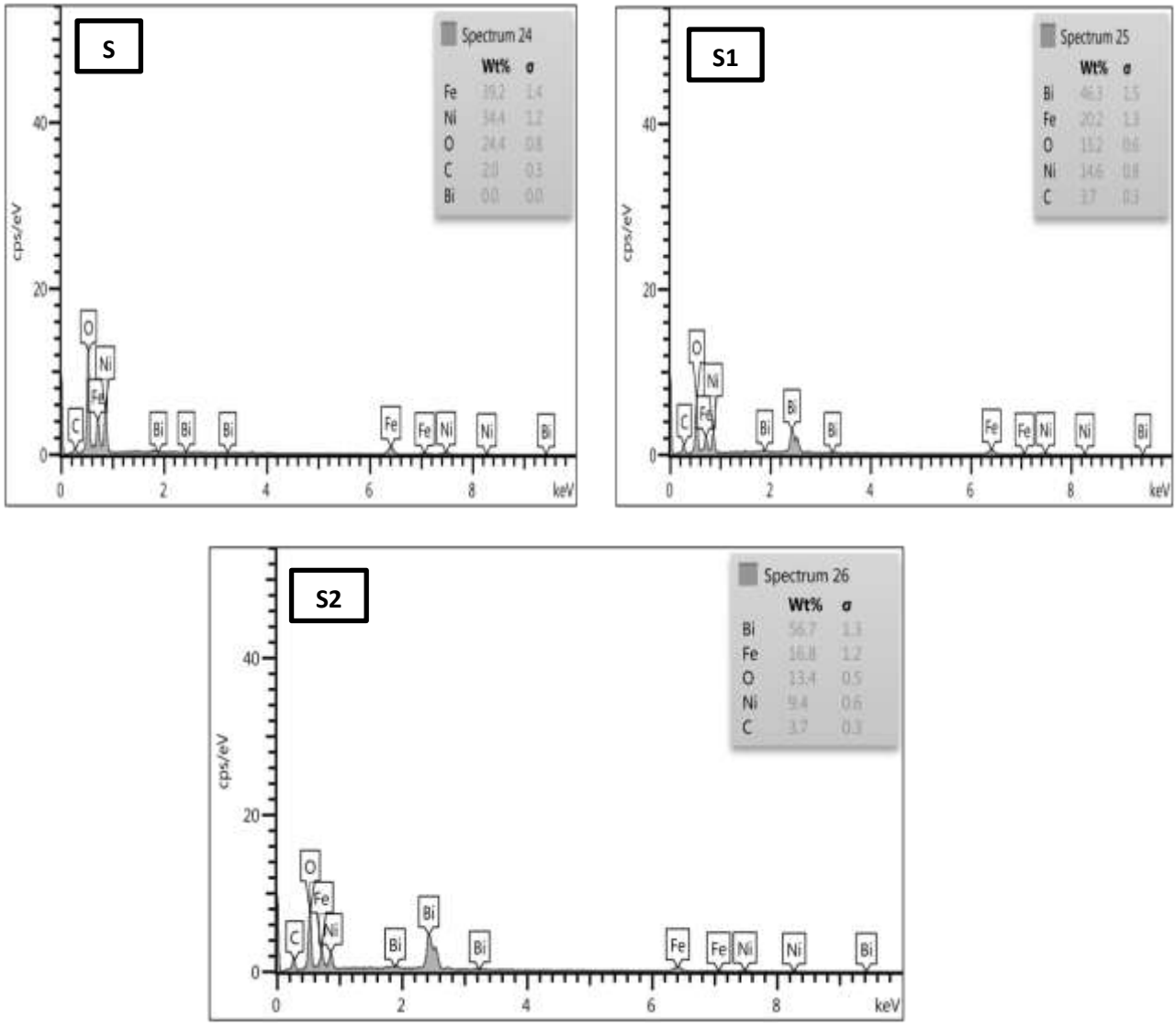

Figure 4: The EDS pattern of ($Bi_xNi_{1-x}Fe_2O_4$/C) nano ferrite particles sintered at 350˚C with the composition (x = 0.0, 0.3 and 0.5)

Academic Science Journal

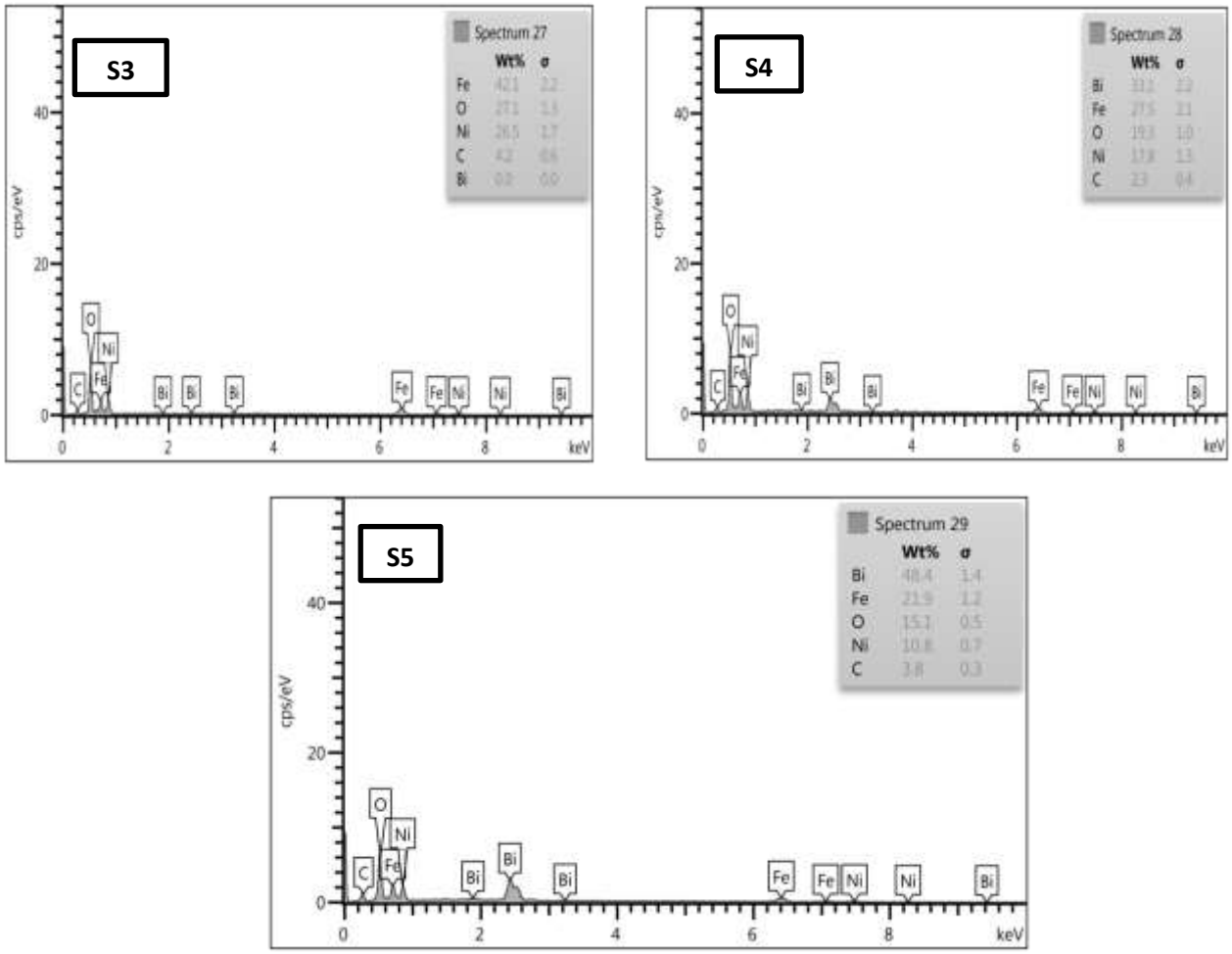

Figure 5: The EDS pattern of ($Bi_xNi_{1-x}Fe_2O_4$/C) nano ferrite particles sintered at 650˚C with the composition (x = 0.0, 0.3 and 0.5)

VSM Analysis

Magnetic measurements were conducted at a standard room temperature of 300 K on samples of [Bi_x Ni $_{1-x}Fe_2O_4$/C]. Figures (6,7) (A and B) depict the magnetization against applied magnetic field (M-H) curves of condensed nanoparticles of [Bi_x Ni $_{1-x}Fe_2O_4$/C] in bulk form. All of the samples exhibit a minimal level of coercivity and remanent magnetization. The study determined the presence of unobstructed superparamagnetic nanoparticles. When the temperature above the blocking temperature [20]. This alignment leads to the formation of a single domain magnetic nanoparticle. Additionally, the coercive force (Hc) was determined

based on the characteristics of the hysteresis loop. The figures (6) and (7) demonstrate a decrease in the coercive force as the value of (x) increases. This variation in coercive force can be explained by the relationship ($H_c=K_t/M_s$), where K_t represents the stability of symmetry. The reduced in (H_c) can be attributed to the small size. The decrease in granularity and roughness can be attributed to the rise in particle size, which in turn enhances the roughness and thus promotes greater stability of the magnetic field walls [21].

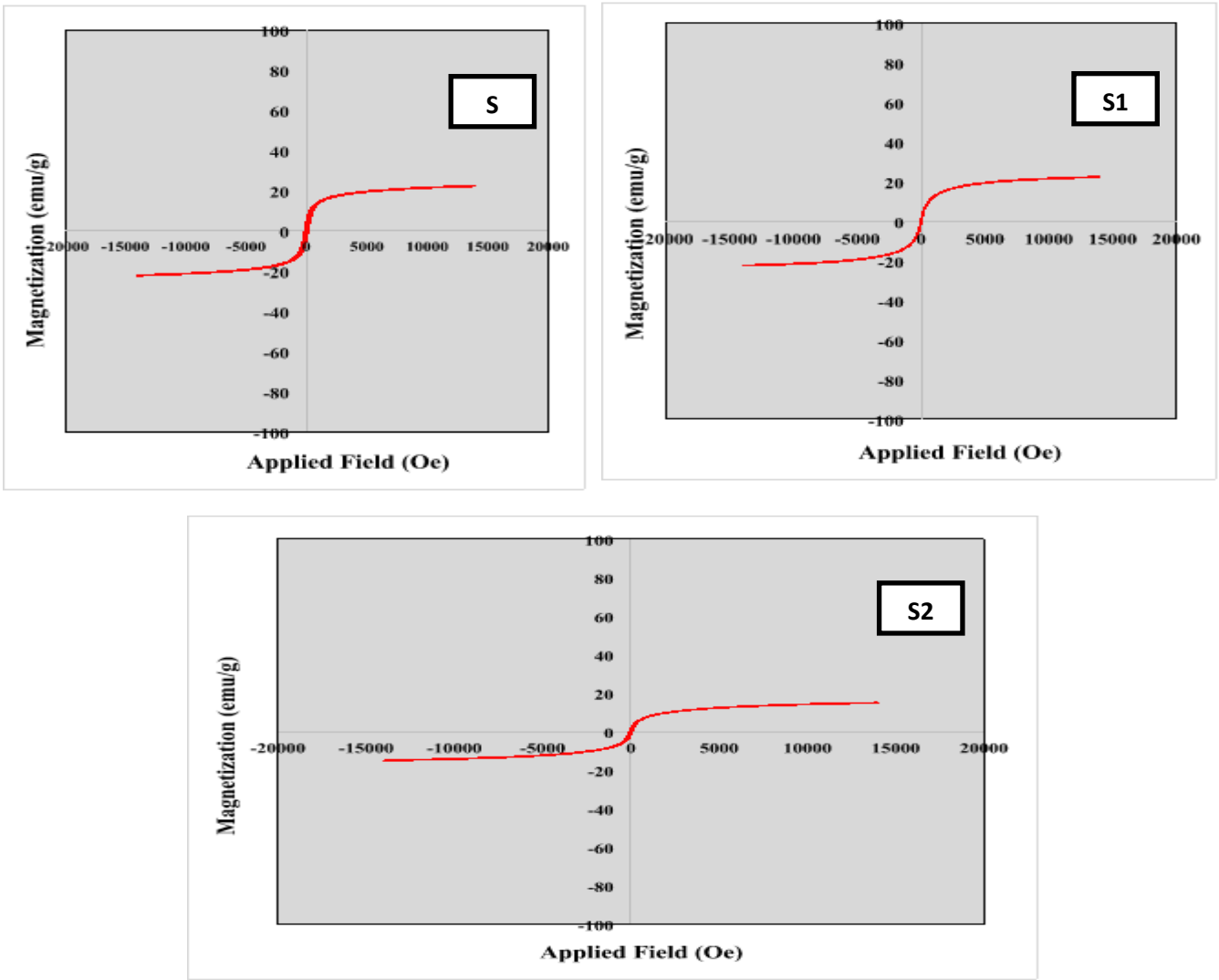

Figure 6: Magnetization versus applied magnetic field of ($Bi_xNi_{1-x}Fe_2O_4/C$) nano ferrite particles sintered at 350˚C with the composition (x = 0.0, 0.3 and 0.5).

Academic Science Journal

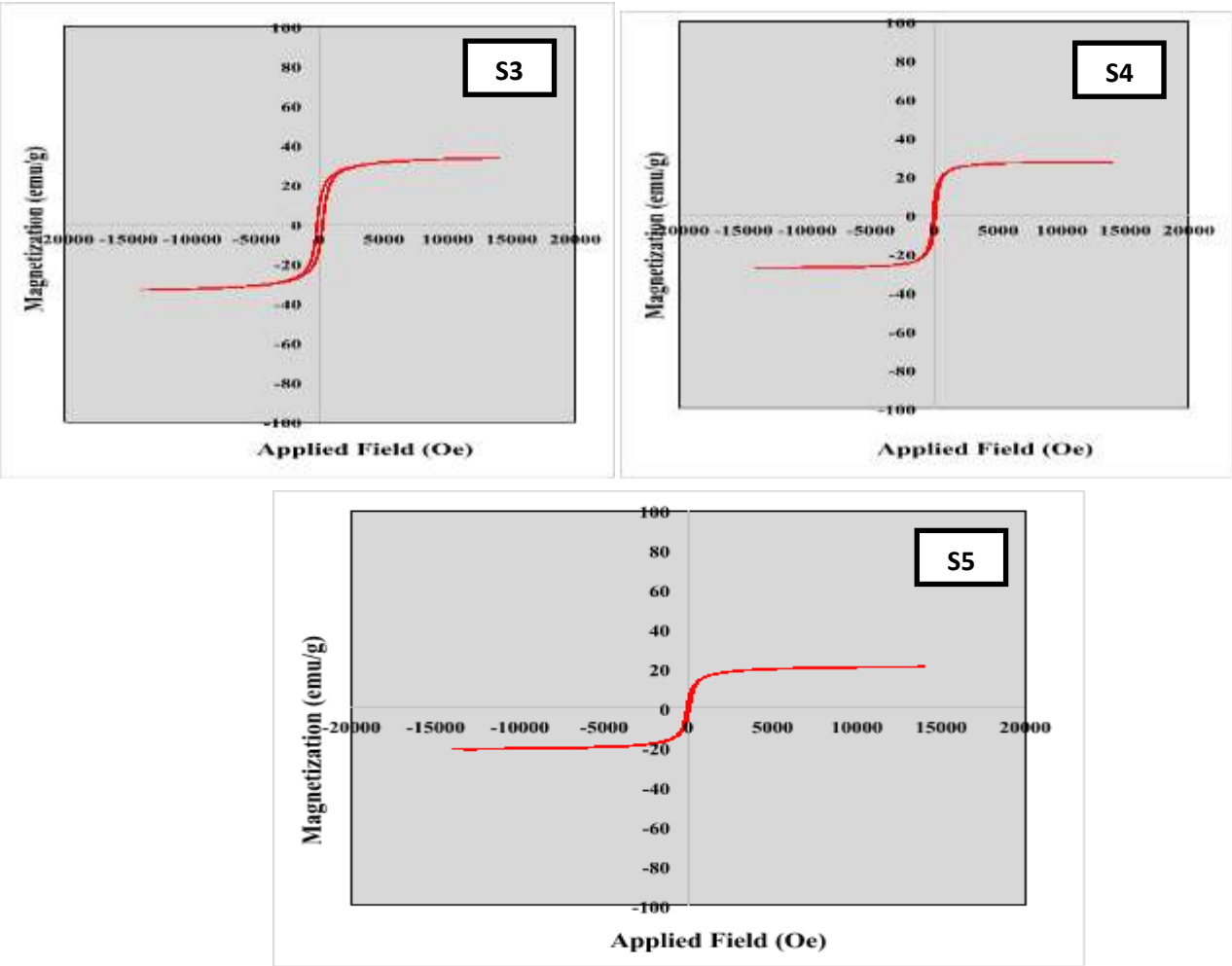

Figure 7: Magnetization versus applied magnetic field of ($Bi_x Ni_{1-x} Fe_2 O_4$/C) nano ferrite particles sintered at 650˚C with the composition (x = 0.0, 0.3 and 0.5)

Table 3: The variation of magnetic parameters for $Bi_x Ni_{1-x} Fe_2 O_4$/C) nano ferrite particles.

Calcination Temperature (°C)	Sample	Hc(Oe)	Mr(emu/g)	Ms(emu/g)	Mr/Ms
350 °C	S	100	7.7	15.89	0.48
	S1	0	2.81	15.69	0.17
	S2	0	2.5	9.27	0.26
650 °C	S3	195	13.07	25.25	0.51
	S4	100	11.82	21.68	0.54
	S5	100	4.83	14.57	0.33

Conclusions

Based on the results of structural (XRD and FTIR) and morphological (FESEM and EDX) experiments, can say the following: (i) The sol-gel auto-combustion method was used to make activated carbon on bismuth nickel ferrite nanoparticles, and it worked well. Careful planning and small changes to the synthesis process lead to the development of a better structure, leading to better structural and morphological traits. (ii) the sharp peaks of the XRD patterns symbolize the high crystallinity of the synthesized samples. (iii) The FTIR spectrum shows that the sample is made of ferrite because it has two strong absorption bands. (iii) The FESEM showed nanoscale size and virtually homogenous particle size distribution, microscopy of activated carbon replaced ferrite shows that the substitution changed the microstructure, resulting in agglomerations of homogenous spherical and other polyhedral particles. The elemental% and atomic% data of activated carbon on bismuth nickel ferrite system reveal the existence of C, Fe, O, Ni, and Bi as participating cations (except when x = 0). Based on the results of a magnetic test, the investigation revealed that the particles exhibited behavior consistent with super paramagnetism due to their suitably small size.

References

1. J. Zhang, L. Wang, Q. Zhang, Hydrothermal carbonization synthesis of $BaZn_2Fe_{16}O_{27}$/carbon composite microwave absorbing materials and its electromagnetic performance, Journal Materials Science, 26, 2538–2543(2015)
2. X. Chen, X. Wang, L. Li, S. Qi, Preparation and microwave absorbing properties of nickel-coated carbon fiber withpolyaniline via in situ polymerization, Journal Materials Science , 27, 5607–5612(2016)
3. T. Zhang, S. Zeng, G. Wen, J. Yang, Novel carbon nanofibers build boron carbonitride porous architectures with microwave absorption properties, Microporous Mesoporous Materials , 211, 142–146(2015)
4. P. I. Liu, L. C. Chung, H. Shao, T. M. Liang, R. Y. Horng, C. M. Ma, M. C. Chang, Microwave-assisted ionothermal synthesis of nanostructured anatase titanium

dioxide/activated carbon composite as electrode material for capacitive deionization, Electrochimica Acta , 96, 173–179(2013)

5. P. I. Liu, L. C. Chung, C. H. Ho, H. Shao, T. M. Liang, R.Y. Horng, M.C. Chang, C. M. Ma, Effects of activated carbon characteristics on the electrosorption capacity of titanium dioxide/ activated carbon composite electrode materials prepared by a microwave-assisted ionothermal synthesis method, Journal of Colloid and Interface Science, 446, 352–358(2015)
6. H. Y. He, Photocatalytic degradations of Malachite Green on magnetically separable Ni_{1-x} Co_x Fe_2 O_4 nanoparticles synthesized by using a hydrothermal process, American Chemical Science Journal, 6, 58-68(2015)
7. D. Zhang, X. Pu, K. Du, Y. M. Yu, J. J. Shim, P. Cai, S. Kim, H. J. Seo, Combustion synthesis of magnetic Ag/$NiFe_2$ O_4 composites with enhanced visible-light photocatalytic properties, Separation and Purification Technology, 137, 82– 85(2014)
8. F. Moeinpour, A. Alimoradi, M. Kazemi, Efficient removal of Eriochrome black-T from aqueous solution using $NiFe_2$ O_4 magnetic nanoparticles, Journal of Environmental Health Science & Engineering, 12, 112-117(2014)
9. P. Mathumba, D. M. Fernandes, R. Matos, Metal oxide (Co_3 O_4 and Mn_3 O_4) impregnation into S, N-doped graphene for oxygen reduction reaction (ORR), Materials (Basel), 13,1562-1570(2020)
10. C. Shi, S. Ullah, K. Li, W. Wang , R. Zhang , L. Pan, X. Zhang and J. Zou , "Low-temperature synthesis of ultrasmall spinel $MnxCo_{3-X}$ O_4 nanoparticles for efficient oxygen reduction, Chinese Journal of Catalysis, 41, 1818–1825(2020)
11. D. Hong, Y. Yamada, T. Nagatomi, Catalysis of nickel ferrite for photocatalytic water oxidation using $[Ru(bpy)_3]^{+2}$ and S_2 O_8^{-2}, Journal American Chemical Society, 134, 19572–19575(2012)
12. Z. Yao, J. Ma , T. K. A. Hoang, High performance biomassderived catalysts for the oxygen reduction reaction with excellent methanol tolerance, International Journal of Hydrogen Energy, 45, 27026–27035(2020)

13. M. A. Gondal, Q. A. Drmosh, Z. H. Yamani, T. A. Saleh, Synthesis of ZnO_2 Nanoparticles by Laser Ablation in Liquid and their Annealing Transformation in to ZnO Nanoparticles, Applied Surface Science, 256(1), 298-304(2009)
14. K. K. Hazarika, C. Goswami, H. Saikia, Cubic Mn_2 O_3 nanoparticles on carbon as bifunctional electrocatalyst for oxygen reduction and oxygen evolution reactions, Molecular Catalysis, 451, 153–160(2018)
15. A. Silambarasu, A. Manikandan, K. Balakrishnan, Comparative study of structural, morphological, magneto-optical and photo-catalytic properties of magnetically reusable spinel $MnFe_2$ O_4 nano-catalysts, Journal of Nanoscience and Nanotechnology, 18, 3523–3531(2018)
16. Y. J. Choi, H. O. Mohamed, S. G. Park, Electrophoretically fabricated nickel/nickel oxides as cost effective nanocatalysts for the oxygen reduction reaction in air-cathode microbial fuel cell, International Journal of Hydrogen Energy, 45, 5960–5970(2020)
17. S. M. Lee, C. S. Lalhmunsiama, Manganese and iron oxide immobilized activated carbons precursor to dead biomasses in the remediation of cadmium-contaminated waters, Environmental Science and Pollution Research, 20, 7464–7477(2013)
18. A. Kim, N. Muthuchamy, C. Yoon, MOF-derived Cu@ Cu_2 O nanocatalyst for oxygen reduction reaction and cycloaddition reaction, Nanomaterials, 8, 1–13(2018)
19. E. M. Kock, M. Kogler, T. Bielz,B. Klotzerand S. Penner, In situ FT-IR spectroscopic study of CO_2 and CO adsorption on Y_2 O_3, ZrO_2, and yttria-stabilized ZrO_2, Journal Physical Chemistry C, 117, 17666–17673(2013)
20. Vahak Marghussian, Nano-Glass Ceramics: Processing, Properties and Applications, (William Andrew, 2015)
21. M. J. Byrne, S. V. Coker, E. Cespedes, P. L. Wincott, D. J. Vaughan, R. A. D. Pattrick, G. Laan, E. Arenholz, F. Tuna, M. Bencsik , J. R. Lloyd, N. D. Telling, Biosynthesis of Zinc Substituted Magnetite Nanoparticles with Enhanced Magnetic Properties, Advanced Functional Materials, 24, 2518–2529(2014)